Inorganic Chemistry

pubs.acs.org/IC

Article

$(CN_3H_6)[Fe^{II}Fe^{III}(SO_4)_3(H_2O)_3]$: A Framework Iron Sulfate with a Mixed $S = 2$ and $S = 5/2$ Honeycomb Lattice

Victoria A. Ginga, Oleg I. Siidra,* Alexander A. Tsirlin, Annette Setzer, Dmitri O. Charkin, Martin Börner, Veronika R. Abdulina, Semen A. Ivanov, Darya A. Gorbachevskaya, and Nikita A. Zolotov

Cite This: https://doi.org/10.1021/acs.inorgchem.3c02109

Read Online

ACCESS | Metrics & More | Article Recommendations | Supporting Information

ABSTRACT: A new guanidinium-templated hydrated iron sulfate, $[CN_3H_6][Fe^{II}Fe^{III}(SO_4)_3(H_2O)_3]$ (**1**), was prepared from strongly acidic aqueous solutions. Its crystal structure is comprised from $Fe^{III}O_6$ and $Fe^{II}O_3(H_2O)_3$ octahedra linked by sulfate bridges forming a $[Fe^{II}Fe^{II}(SO_4)_3(H_2O)_3]^-$ 3*D* framework with a layer-by-layer ordering of ferric and ferrous cations. The structural topology of the framework is related to the anhydrous rhombohedral mikasaite $Fe_2(SO_4)_3$. The removal of part of the sulfate tetrahedra and the partial replacement of the Fe^{3+} cations in the $[Fe^{3+}{}_2(SO_4)_3]^0$ framework by Fe^{2+} provide a negative charge and allow the incorporation of the protonated organic species in the voids. The compound **1** has been characterized by single-crystal X-ray diffraction, TG and DSC analyses, UV−vis−NIR spectroscopy, magnetic susceptibility, Mössbauer spectroscopy, IR and Raman spectroscopy, and density functional band-structure calculations. The magnetic behavior of **1** shows an interplay of Fe^{II} ($S = 2$) and Fe^{III} ($S = 5/2$) sublattices that exhibit different types of antiferromagnetic couplings, one Fe^{III}−Fe^{III} ($J_1 \sim 6.1$ K) and two Fe^{II}−Fe^{III} couplings ($J_2 \sim 1$ K, $J_3 \sim 5.9$ K) within corrugated honeycomb layers. These ferrimagnetic layers are coupled antiparallel to each other, resulting in an overall antiferromagnetic order below $T_N = 31$ K.

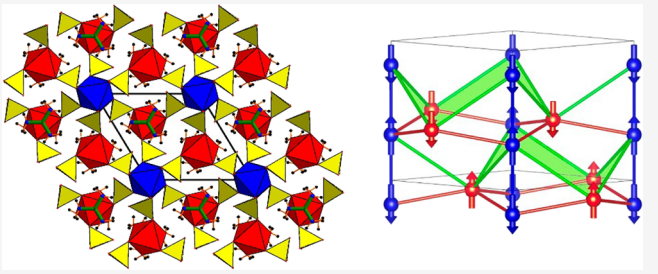

INTRODUCTION

Hydrated iron sulfates are some of the most widely represented and studied objects among natural and synthetic compounds. These compounds play a significant role in chemical, biological, and geological processes.[1,2] The iron (II and III) and sulfate ions are one of the most common constituents of the lithosphere[3] and have been recently detected in extraterrestrial environments.[4−6] Moreover, the sulfate anion is a strong kosmotropic molecule in terms of a Hofmeister series.[7] Prone to the loss of one electron in an isolated state,[8−10] the sulfate species are very stable in the condensed state in the presence of counterions or solvent environment.[11] Despite the active study of hydrated iron sulfates, the chemical, thermal, and magnetic behaviors of these compounds templated by organic species are less studied.[12]

The guanidinium cation $[C(NH_2)_3]^+$ is a planar and strongly basic[13] template and a potential donor of up to six relatively strong hydrogen bonds; it is actively employed in the synthesis of organo-inorganic compounds,[14−16] including noncentrosymmetric structures.[17,18] When considering iron organo-inorganic compounds, magnetic properties also are an important focus of the scientific research.[19−21] In this regard, of essential interest are the cation-ordered structures incorporating both Fe^{II} ($S = 2$) and Fe^{III} ($S = 5/2$). Among sulfate minerals, such Fe^{II}/Fe^{III} ordering has been reported for römerite, $Fe^{II}Fe^{III}{}_2(SO_4)_4{\cdot}14H_2O$[22], and voltaite, $K_2Fe^{II}{}_5Fe^{III}{}_3Al(SO_4)_{12}{\cdot}18H_2O$.[23] Yet, the overwhelming majority of synthetic organo-inorganic iron sulfates are based on Fe^{2+};[24,25] a single organically templated mixed-valence iron sulfate, $[(CH_3)_2(NH_2)]_6(Fe^{III}{}_4Fe^{II}{}_2(O)_2(OH)_2(SO_4)_8]$, has been reported.[26] Such mixed-valence architectures are also of interest for the design of complex magnetic systems, including frustrated magnets with intriguing ground states. The combination of Fe^{II} and Fe^{III} as two different magnetic ions opens further possibilities, including creation of ferrimagnets with compensation points and exchange bias.[26−28]

Herein, we report the synthesis of a new compound $[CN_3H_6][Fe^{II}Fe^{III}(SO_4)_3(H_2O)_3]$ (**1**), the first guanidinium-templated hydrated iron sulfate with mixed spins $S = 2$ and $S = 5/2$, and discuss its structural, magnetic, and other properties.

EXPERIMENTAL SECTION

Synthesis. Initially, several single crystals of **1** (Figure 1) were observed during an attempt to prepare a guanidinium iron(II) sulfate; just a couple of large very dark hexagonal platelets were formed,

Received: June 25, 2023

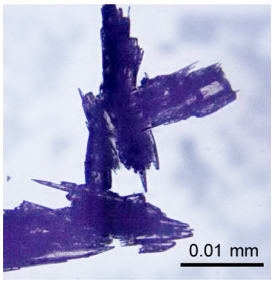

Figure 1. Crystal clusters of **1** under an optical microscope.

presumably due to the partial oxidation of ferrous iron by atmospheric oxygen. After the X-ray structure determination (see below), a bulk sample could be prepared. Metallic iron was dissolved in a 10-fold excess of 20% sulfuric acid upon heating the solution to 40−50 °C. A solution of ferric iron sulfate $Fe_2(SO_4)_3{\cdot}9H_2O$ and solid guanidinium sulfate $(CN_3H_6)_2SO_4$ was added so that the $[CN_3H_6]^+$:Fe^{II}:Fe^{III} molar ratio in the mother liquor was 1:1:1. The resulting light yellow solution was evaporated at room temperature. After its initial volume was reduced to about one-third, its color turned into intense gray and formation of a dark polycrystalline precipitate was observed. After the crystallization, the solution completely discolored. The precipitate was mechanically separated from the walls of the glass, washed with cooled 20% sulfuric acid, and dried on a Schott filter. It is readily decomposed in distilled water with the formation of fine off-white precipitate, probably hydrolysis products. Under mother liquor or in closed vials, **1** is stable for at least 6 months.

Single-Crystal X-ray diffraction. A single crystal of **1** was selected for X-ray diffraction data collection and mounted on a thin glass fiber and tested on a Rigaku XtaLAB Synergy-S diffractometer equipped with a PhotonJet-S detector operating with Mo Kα radiation at 50 kV and 1 mA. More than a hemisphere of three-dimensional XRD data was collected with frame widths of 0.5° in ω and a 30 s count time for each frame. The collected data were integrated and corrected for absorption using a multiscan type model using the CrysAlis software. The crystal structure of **1** was further refined in the $P6_3$ space group to R_1 = 0.030 (wR_2 = 0.061) for 1196 reflections with $|F_0| \geq 4\sigma F$ by using the SHELX software.[29] General crystallographic information is given in Table 1. All atoms except for hydrogens were refined anisotropically. All H atoms were located from the analysis of difference Fourier electron density maps and were refined with imposed O−H and N−H distance restraints of 1.00 ± 0.02 Å. Bond-valence sums and anisotropic displacement parameters for all atoms are given in Tables S1 and S2, respectively. Selected interatomic distances are listed in Table 2.

Table 1. Crystallographic Data and Refinement Parameters for 1

crystal size (mm)	0.08 × 0.08 × 0.05
space group	$P6_3$
a (Å)	9.1976(5)
c (Å)	9.1060(6)
V (Å^3)	667.12(8)
μ (mm^{-1})	2.741
D_{calc} (g/cm^3)	2.559
radiation wavelength (Å)	0.71073 (Mo Kα)
θ-range (deg.)	3.398−33.434
total ref.	4918
unique ref.	1380
unique $\|Fo\| \geq 4\sigma F$	1196
R_{int}	0.040
R_1	0.030
GoF	1.084
CCDC	2265854

Table 2. Selected Bond Lengths (in Å) in the Structure of 1

Fe1−O1	1.974(3) × 3	S1−O2	1.450(3)
Fe1−O3	2.014(3) × 3	S1−O4	1.465(2)
<Fe1−O>	1.994	S1−O1	1.491(4)
		S1−O3	1.492(3)
Fe2−O4	2.117(3) × 3	<S1−O>	1.474
Fe2−O_w1	2.158(3) × 3		
<Fe2−O>	2.1375	C1−N1	1.327(4) × 3

Powder X-ray Diffraction. XRD data used for profile matching analysis of **1** was recorded in the 2θ range of 10−90° with a step size of 0.02° using a Bruker "D2 Phaser" diffractometer (Co Kα radiation, λ = 1.7889 Å). The profile matching analysis was carried out in the JANA2006 crystallographic system.[30] A comparison of the structural data of the single-crystal experiment with the data of powder diffraction was performed by the Rietveld method.[31] The background was fitted using the Chebyshev polynomial function, and the peak shapes were described by a pseudo-Voigt function. The refined unit cell parameters in the space group $P6_3$ are a = 9.1984(1) Å and c = 9.1113(1) Å. The final observed and calculated powder XRD patterns are given in Figure S1. The parameters of the full-profile Rietveld refinement are collected in Table S3.

IR and Raman Spectroscopy. The Infrared (IR) spectrum of the polycrystalline sample of **1** was acquired on a Bruker Vertex 70 FTIR infrared Fourier spectrometer in the range 4000−400 cm^{-1} with a resolution of 4 cm^{-1}. The sample was mixed with a predried KBr and pressed into a pellet. The obtained spectra (Figure S2 and Table S4) were processed using the Opus software (Bruker Optik, 2004).

The Raman spectrum of **1** was acquired on a Horiba Jobin-Yvon LabRam HR800 spectrometer equipped with an Ar^+ laser (λ= 514 nm) at 50 mW output power and ∼6 mW power at the sample surface for an area of 2 × 2 μm. The Raman spectrum was recorded at room temperature from randomly oriented crystalline aggregates placed on a glass slide and further processed using LabSpec (Horiba) and Origin software. The results are given in the Supporting Information.

UV−vis−NIR Spectroscopy. The diffuse reflectance spectrum was collected at room temperature on a Jasco V-670 UV−vis−NIR spectrophotometer with an ARN-914 absolute reflectance measurement unit equipped with a photomultiplier and a PbS photoconductive cell. The spectrum was collected in the 200−1400 nm range with a resolution of 2 nm. $BaSO_4$ was used as a reference material. The sample was optically diluted with $BaSO_4$ (5 wt % sample). Diffuse reflectance UV−visible data are frequently analyzed using a normalized absorbance, which is referred to as the Kubelka−Munk function,[32] $f(R_\infty)$, given by:

$$f(R_\infty) = \frac{(1 - R_\infty)^2}{2R_\infty} = \frac{K}{S}$$

where R, the diffuse reflectance of a sample, is related to the absorption coefficient (K) and its scattering coefficient (S). Assuming the scattering coefficient is independent from the wavelengths, $f(R_\infty)$ is directly proportional to the absorption of the sample.

Thermal Analysis (TG + DSC). Thermal analysis was performed on a NETZSCH STA 449 CD in the range of 30−500 °C. Fourteen milligrams of powder sample was placed in an alumina crucible covered with a lid. The heating rate was 10 °C/min with an air flow of 50 mL/min. The obtained data with a description are given in the Supporting Information (Figure S3).

Mössbauer Spectroscopy. ^{57}Fe Mössbauer spectra were measured at room temperature using an SM 2201 Mössbauer spectrometer recording γ radiation in the transmission geometry. The reference signal in the spectrometer Doppler modulator had a sawtooth shape to set the velocity with a constant acceleration. The source of γ-quanta was ^{57}Co with an activity of 15 × 10^8 Bq. The velocity scale was calibrated using a 6 μm thick α-Fe foil.

Magnetization Measurements. The field-dependent magnetization and temperature-dependent magnetic susceptibility were measured on a polycrystalline sample with a total mass of 24.3 mg.

https://doi.org/10.1021/acs.inorgchem.3c02109
Inorg. Chem. XXXX, XXX, XXX−XXX

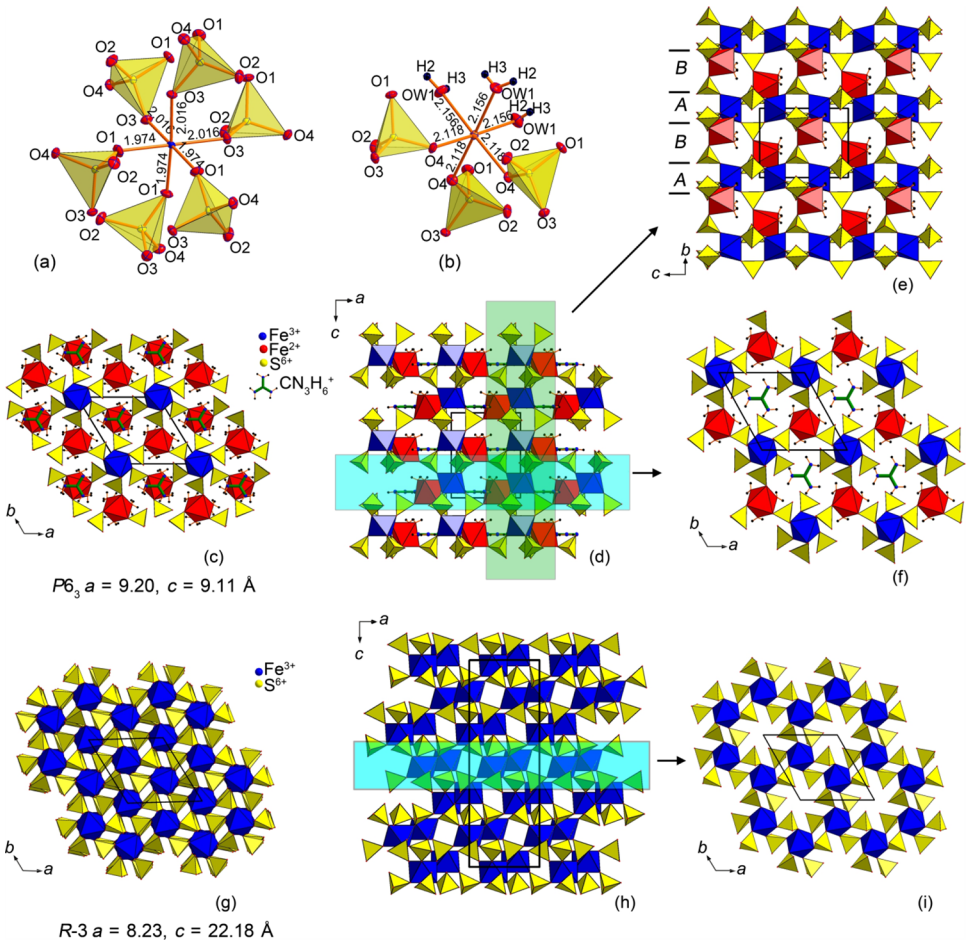

Figure 2. Coordination environments of (a) Fe1^{3+}, (b) Fe2^{2+}, and S^{6+} cations in the structure of **1**. General projection of the crystal structure of **1** along the (c, d) *c* and *b* axes. (e, f) The structure can be split into 2D blocks. (f) The voids are occupied by guanidinium cations. (e) Layer-by-layer ordering of ferric and ferrous iron cations in the structure of **1**. (g, h) General projections of the crystal structure of rhombohedral $Fe_2(SO_4)_3$ (mikasaite). (i) The framework can be split into layers with empty voids.

Direct current (dc) and alternating current (ac) magnetic susceptibility measurements were performed in the temperature range of 2−300 K in magnetic fields up to 7 T using the MPMS-XL magnetometer from Quantum Design. The sample chamber was flushed with helium gas and evacuated to about 10^{-2} atm. In ZFC measurements, zero magnetic field was set using the oscillating mode. Measurements of the ac susceptibility were performed upon zero-field cooling at frequencies of 0.1, 1, 10, and 500 Hz with the amplitude of 0.3 mT in the presence of a constant magnetic field of 0.01 T.

Ab Initio Calculations. Magnetic exchange couplings in **1** were obtained from relativistic density functional theory (DFT) band structure calculations performed in the VASP code[33,34] using Perdew−Burke−Ernzerhof type of the exchange correlation potential.[35] Correlation effects in the Fe 3*d* shell were taken into account on the mean-field DFT + *U* level with the on-site Coulomb repulsion parameter U_d = 6 eV and Hund's coupling J_d = 1 eV.[36] Individual exchange parameters J_i normalized per bond were extracted by a mapping procedure from total energies of four collinear spin configurations.[37] Experimental structural parameters and k-mesh with 64 points in the first Brillouin zone were used.

RESULTS

Crystal Structure. The crystal structure of **1** contains two symmetrically independent iron sites, Fe1 (Fe^{III}) and Fe2 (Fe^{II}), and one S site (Figure 2a). The coordination environment of the ferric Fe1 site is formed by three O1 and three O3 atoms with bond lengths of 1.974(3) and 2.014(3) Å, respectively, thus forming the $Fe1O_6$ octahedra. The ferrous Fe2 site is octahedrally coordinated by three O4 and three O_w1 water oxygens at distances of 2.117(3) and 2.158(3) Å, respectively. The bond valence sums for the Fe−O bonds agree well with the expected oxidation states of 3+ and 2+ for the Fe1 and Fe2 sites, respectively (Table S1).

The S site is surrounded by four oxygen atoms O1, O2, O3, and O4 with the formation of the sulfate tetrahedral complex SO_4. The S−O bond lengths in the range of 1.450(3) to 1.492(3) Å and the angles of 106.5(2) to 113.3(2)° fall within the range typically observed among sulfate structures.

The C1 site is trigonally coordinated by the NH_2 groups according to the planar equidistant $[C(NH_2)_3]^+$ geometry.

The octahedron of the $Fe1^{III}$ site is coordinated by six monodentate sulfate tetrahedra via common oxygen vertices of O1 and O3 (Figure 2a); the octahedron of the $Fe2^{II}$ site is connected with three sulfate anions only through the O4 oxygen vertices and three water molecules, as shown in Figure 2b. The sulfate groups bridge the ferric and ferrous octahedra.

The overall architecture of **1** (Figure 2c−f) corresponds to a new structure type related to anhydrous rhombohedral $Fe_2(SO_4)_3$ (mikasaite)[38] (Figure 2g−i). The $Fe1O_6$ and $Fe2O_3(H_2O)_3$ octahedra share no common edges or vertices, yet they are linked via the bridging sulfate groups thus forming hexagonal pseudolayers further interconnected into the 3*D*

https://doi.org/10.1021/acs.inorgchem.3c02109
Inorg. Chem. XXXX, XXX, XXX−XXX

$[Fe^{II}Fe^{III}(SO_4)_3(H_2O)_3]^-$ framework. The water molecules serve as terminating ligands at the $Fe2^{II}$ site. The guanidinium cations reside in the cavities of the framework and form hydrogen bonds to the terminal oxygen atoms of sulfate groups; yet, their structure-driving role is evident since attempts to replace these cations by a Cs^+ cation of comparable size but of quite dissimilar shape resulted only in crystallization of $CsFe(SO_4)_2{\cdot}12H_2O$ alum. The structure of **1** can be split into 2*D* blocks depending on the direction. Along the *a* axis, $Fe2O_3(H_2O)_3$ and $Fe^{III}O_6$ octahedra form alternating sublayers *A* and *B*, respectively (Figure 2e). The *a* parameter is significantly enlarged in the structure of **1** comparing to $Fe_2(SO_4)_3$ archetype (Figure 2g–i). The cavities are empty in $Fe_2(SO_4)_3$ (Figure 2i), whereas they are filled by $[C(NH_2)_3]^+$ in **1** (Figure 2f).

The hydrogen bonding separations in **1** are presented in Table S5 and Figure S4. The donors are the O_w1 and N atoms, and the acceptors are the O1, O2, O3, O4, and O_w1 atoms. The guanidinium cations interact with the iron-sulfate framework layer via the N1–H1···O2/O1 and N1–H4···O_w1/O2/O4 contacts. The presence of hydrogen bonds determines the strength of chemical interactions between the organic $[C(NH_2)_3]^+$ cation and the anionic inorganic framework.

UV–vis–NIR Spectroscopy. The UV–vis absorbance spectrum of **1** revealed three absorbance peaks at 306, 430, and 538 nm (Figure 3). Additionally, two broad absorptions at

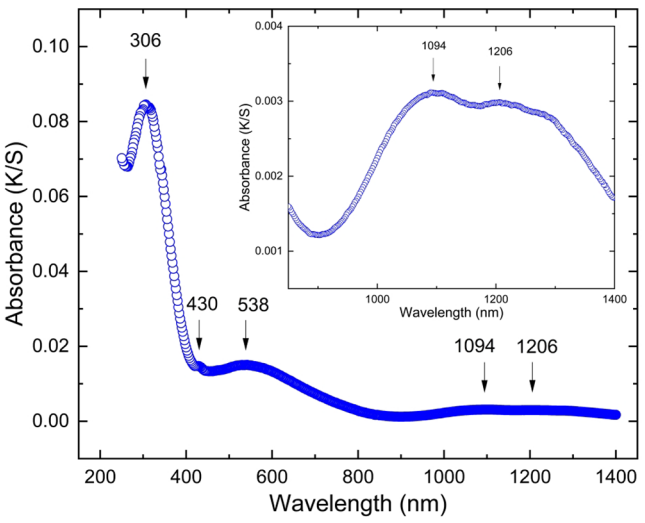

Figure 3. UV–vis spectrum of **1**.

1094 and 1206 nm could be detected in the NIR range. The first very intense band is centered near UV and extends onto the lower wavelengths of the visible region. This absorption can be attributed to the charge transfer (LMCT) transition from the oxygen ligands to the metal ions.[39] Beside the contribution of the Fe^{2+} LMCT (higher energy) and Fe^{3+} LMCT (lower energy), the broad absorption band has a shoulder at 430 nm, which can be attributed to the formally spin-forbidden $^6A_{1g}$–$^4A_{1g}$, ^4E_g transitions of a Fe^{III} (d^5).[39,40] The remaining absorption band in the visible spectrum with a maximum at 538 nm can be explained by the $^6A_{1g}$–$^4T_{2g}$ ligand field transition of Fe^{III} ions. For an octahedral high-spin Fe^{II} (d^6), only one $^5T_{2g}(D)$–^5E_g allowed transition is expected in the NIR region. Due to a dynamic Jahn–Teller effect in the excited ^5E state, a splitting of the $^5T_{2g}(D)$–^5E_g absorption band typically occurs.[41] The spectrum for $[Fe(H_2O)_6]^{2+}$ in aqueous solution, for example, reveals two components at 962 and 1204 nm of the $^5T_{2g}(D)$–^5E_g transition. This comparison suggests that the low-intensity NIR bands at 1094 and 1206 nm seen in the spectrum of **1** arise from ligand field transitions involving Fe^{III} high-spin ions. For mixed valent $Fe^{II/III}$ materials, intervalence charge transfer (IVCT) can occur. In sites of near-octahedral coordination, this transition is found in the 630–820 nm region.[39] Although there is no obvious IVCT band in the spectrum of **1**, there might be a weak contribution to the broad absorption located in the 550–800 nm range. Further temperature-dependent spectral measurements preferably on single crystals and detailed analysis of the ligand field transitions as well as theoretical calculations might be necessary to unambiguously identify the origin of these transitions.

The data obtained from the UV–vis–NIR spectrum of **1** in combination with the results of analysis of the crystal structure, as well as Mössbauer spectroscopy, make it possible to divide Fe^{III} and Fe^{II} into two independent sites Fe1 and Fe2, respectively. Minor deviations in the calculated bond valence sum may also suggest intervalence charge transfer between Fe sites, presumably related to class II.[42]

Mössbauer Spectroscopy. Table 3 presents the hyperfine interaction parameters, and Figure 4 shows the Mössbauer

Table 3. Mössbauer Spectral Parameters for Octahedrally Coordinated Fe in 1 at RT[a]

component	Fe	δ(mm/s)	Δ(mm/s)	*A* (%)
doublet 1	Fe^{II}	1.281 ± 0.001	1.732 ± 0.002	55.18
doublet 2	Fe^{III}	0.528 ± 0.001	0.021 ± 0.002	44.82

[a] δ is the isomer shift, QS is the quadrupole splitting, and A is the spectral area. Isomeric shifts are given relative to α–Fe.

spectrum of **1**. The spectrum has a complex structure and can be described by a sum of two doublets, doublet 1 and doublet 2 with minimal quadrupole splitting. According to spectral

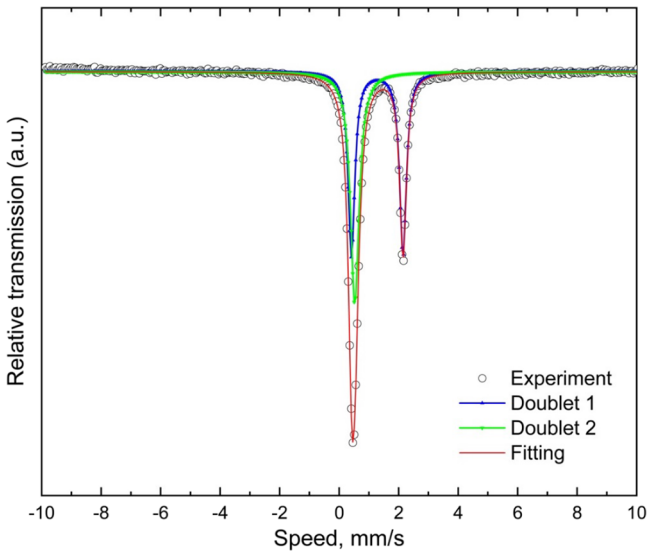

Figure 4. Mössbauer spectrum of **1**. Red, blue, and green solid lines correspond to the calculated total spectrum, doublet 1, and doublet 2, respectively.

https://doi.org/10.1021/acs.inorgchem.3c02109
Inorg. Chem. XXXX, XXX, XXX–XXX

parameters, doublet 1 belongs to Fe^{II} (ferrous) iron in the isolated octahedral site Fe2, and doublet 2 belongs to Fe^{III} (ferric) iron in the isolated octahedral site Fe1 (Fe^{III}). Due to the low quadrupole splitting, the doublet 2 (Fe^{III}) resembles a singlet, which in turn implies that there is only a negligible electric field gradient at the nucleus of the Fe^{3+} cation. Sulfate minerals belonging to the $Fe_2(SO_4)_3{\cdot}nH_2O$ hydration series have similar parameters of the Mössbauer spectra, which includes quenstedtite $Fe_2(SO_4)_3{\cdot}11H_2O$, coquimbite $AlFe_3(SO_4)_6(H_2O)_{12}{\cdot}6H_2O$, kornelite $Fe_2(SO_4)_3{\cdot}7H_2O$, and lausenite $Fe_2(SO_4)_3{\cdot}5H_2O$.[43] For comparison, Huggins and Huffman (1979)[44] reported a doublet with δ = 0.44 mm/s and Δ = 0.15 mm/s for kornelite. Doublet 1 (Fe^{II}) has a rather low value of quadrupole splitting (δ = 1.281 mm/s and Δ = 1.732 mm/s). The lowest values of the Fe^{II} quadrupole splitting belong to voltaite $K_2Fe^{II}{}_5Fe^{III}{}_3Al(SO_4)_{12}{\cdot}18H_2O$, with doublets at δ = 1.15−1.35 mm/s and Δ = 1.58−1.82 mm/s.[43,45] The spectral parameters of **1** are close to those for voltaite, in the crystal structure of which Fe^{II} and Fe^{III} occupy symmetrically independent sites and remain isolated from each other.[46] Our results can also be compared with available data for römerite $Fe^{2+}Fe^{3+}{}_2(SO_4)_4{\cdot}14H_2O$ with δ = 0.52 mm/s, Δ = 0.38 mm/s for Fe^{III} and δ = 1.38 mm/s, Δ = 3.49 mm/s for Fe^{II}.[47] Thus, in addition to the calculated bond valence sums (Table S1) based on the single-crystal X-ray data of **1**, the results of Mössbauer spectroscopy allow us to clearly distinguish Fe^{II} and Fe^{III} in isolated unmixed sites.

Magnetic Behavior. Above 120 K, **1** exhibits paramagnetic behavior with a linear temperature dependence of the inverse susceptibility (Figure 5). The modified Curie−Weiss fit, $\chi = \chi_0 + C/(T - \theta)$, returns the temperature-independent contribution $\chi_0 = -1.7 \times 10^{-4}$ emu/mol, antiferromagnetic Curie−Weiss temperature of $\theta = -52$ K, and Curie constant C = 6.89 emu K/mol, which corresponds to the effective paramagnetic moment of μ = 7.42 μ_B/f.u. in a good agreement with 7.68 μ_B expected for the combination of S = 5/2 Fe^{III} and S = 2 Fe^{II} states. The negative value of the Curie−Weiss temperature indicates that dominant exchange interactions are antiferromagnetic.

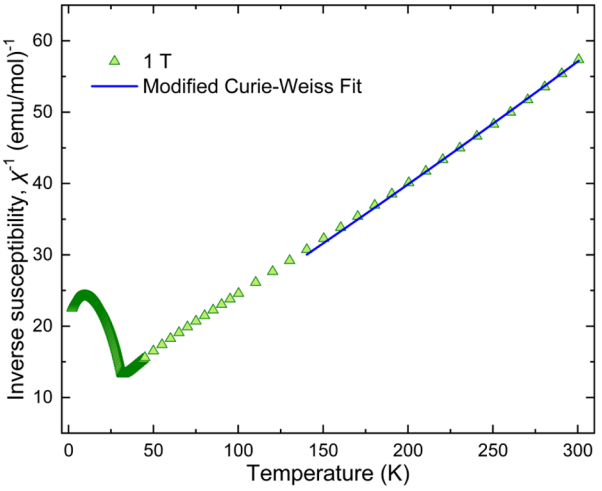

Figure 5. Inverse magnetic susceptibility of **1** measured in the applied field of 1 T. The blue line shows the modified Curie−Weiss fit, $\chi = \chi_0 + C/(T - \theta)$.

Below 100 K, a pronounced anomaly indicative of magnetic ordering is observed at T_N = 31 K in the applied fields of 0.01 and 0.1 T. It is also evident from the peak in Fisher's heat capacity $d(\chi T)/dT$ (Figure 6a). Interestingly, the transition

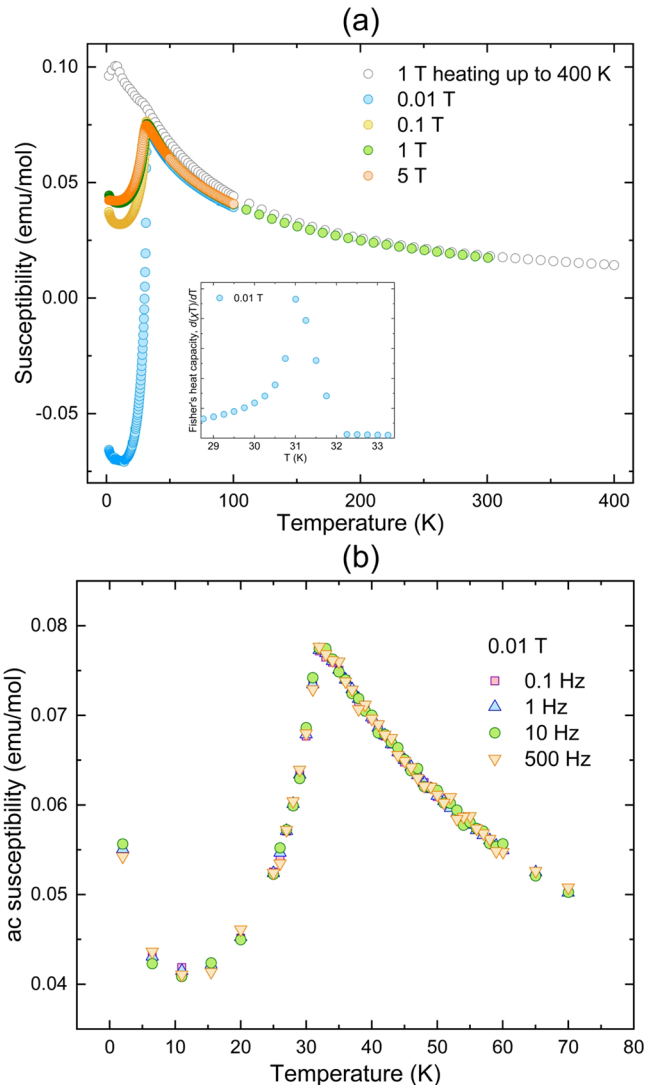

Figure 6. (a) Temperature-dependent magnetic susceptibility of **1** measured in the applied fields of 0.01, 0.1, 1, and 5 T. The inset shows Fisher's heat capacity $d(\chi T)/dT$ calculated based on the 0.01 T susceptibility. (b) AC susceptibility of **1** measured in the applied field of 0.01 T at frequencies 0.1, 1, 10, and 500 Hz.

anomaly almost disappeared when the temperature range of the measurement was extended to 400 K (Figure 6a, pale gray data), probably because of the dehydration that may start already at 400 K when the sample is heated in vacuum. Therefore, the sample temperature was kept below 300 K in all further measurements.

The relatively low frustration ratio of θ/T_N = 1.58 suggests only minor frustration effects. On the other hand, measurement under field-cooled and zero-field-cooled conditions revealed a clear splitting below T_N. Our ac-susceptibility measurements (Figure 6b) do not show any frequency dependence of the peak at T_N and exclude spin freezing (Figure 7). The ac- and dc-data are in good agreement above T_N, while below T_N, the ac-data deviate from both the FC and ZFC dc-data measured at 10 mT (Figure 7) because the susceptibility becomes field-dependent. The ac-susceptibility shows the sample response to a weak oscillating field of 0.3

https://doi.org/10.1021/acs.inorgchem.3c02109
Inorg. Chem. XXXX, XXX, XXX−XXX

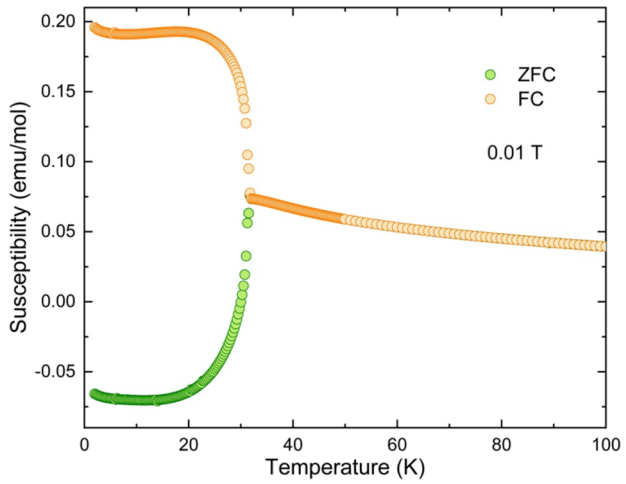

Figure 7. ZFC and FC magnetic susceptibilities of **1** in the applied field of 0.01 T.

mT, whereas the dc-susceptibility is the sample response to the constant field of 10 mT.

Surprisingly, negative magnetic susceptibility was recorded in the field of 0.01 T upon zero-field cooling. Such features are typical for ferromagnets where finite magnetic field is required to align the domains. Whereas no traces of ferromagnetism are observed in **1**, a similar scenario may be possible if the ferrimagnetism of individual honeycomb layers is taken into account (see below). Another interesting observation is that the $M(H)$ curve measured at 2 K, below T_N, shows a small offset from zero (Figure 8) and indicates an exchange bias

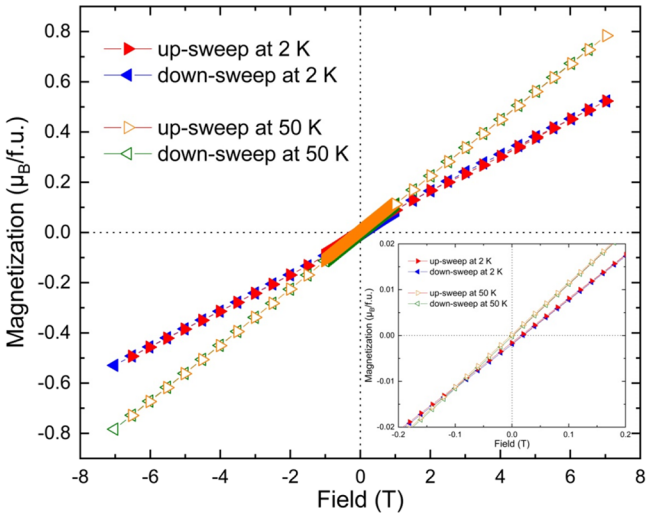

Figure 8. Field-dependent magnetization of the **1** measured at 2 and 50 K. Inset: enlarged data in the vicinity of the origin highlights the small offset of the 2 K data due to the exchange bias effect.

effect.[21,48] Exchange bias has been observed in mixed oxides that combine weakly and strongly anisotropic magnetic ions.[49,50] A similar scenario may be envisaged in our case because Fe^{3+} (d^5) with the quenched orbital moment is isotropic, whereas Fe^{2+} (d^6) with the unquenched orbital moment should be anisotropic. Therefore, two magnetic ions with very different anisotropies are simultaneously present in **1**.

The microscopic magnetic model of **1** was obtained from DFT. Three shortest Fe−Fe distances in the structure are 4.553(2) Å (Fe^{III}−Fe^{III}, J_1), 5.4003(4) Å (Fe^{III}−Fe^{II}, J_2), and 6.399(1) Å (Fe^{III}−Fe^{II}, J_3). According to the results of our ab initio calculations, the magnetism in **1** is dominated by the Fe^{III}−Fe^{III} coupling $J_1 \sim 6.1$ K and the Fe^{III}−Fe^{II} coupling of $J_3 \sim 5.9$ K, whereas $J_2 \sim 1$ K is much weaker; all couplings are antiferromagnetic. The coupling J_3 corresponds to the corrugated honeycomb layers with ferrimagnetic order due to the different magnetic moments of ferric and ferrous cations. These ferrimagnetic layers are interconnected by the AFM interaction J_1 leading to a fully compensated magnetic structure. The J_2 coupling forms triangular loops with J_1 and J_3, thus leading to weak frustration (Figure 9). This may explain the small departure of the frustration ratio θ/T_N from 1.0. The average Curie−Weiss temperature based on the calculated interactions J_1, J_2, and J_3 is −43.6 K in good agreement with the experimental value of −52 K.

A similar arrangement of iron atoms with different oxidation states, and the formation of mixed-spin honeycomb ferrimagnetic layers were also described in Nakamura's work for the series of molecular-based magnets $AFe^{II}Fe^{III}(C_2O_4)_3$ [$A = N(n-C_nH_{2n+1})_4$, $n = 3$−5].[28,51] We note that in both cases, the magnetic centers interact via anionic bridges (sulfate or oxalate), which probably provide the exchange pathways. Such bridges, in the case of sulfates, provide the pathways for charge transfer manifested by the intense coloring while Fe^{n+}·aq is nearly colorless. Besides **1**, there is at least one more example of a strongly colored complex Fe^{II}/Fe^{III} sulfate, the mineral voltaite $K_2Fe^{II}{}_5Fe^{III}{}_3Al(SO_4)_{12}\cdot 18H_2O$, whose structure also contains the Fe^{II}−$SO_4{}^{2-}$−Fe^{III} bridges.[23] The magnetic behavior and Mössbauer spectra of this compound and its derivatives are more complex due to the mixed Fe^{II}/Fe^{III} occupancy of some sites[42] while the structure of **1** exhibits an excellent Fe^{II}/Fe^{III} ordering, with each cation occupying a single site. We also note that both the synthetic analogues of voltaite[42] and the compound **1** were obtained from strongly acidic solutions containing a large excess of sulfate anions. This is probably the necessary condition for substituting, at least partially, the water molecules from the coordination sphere of the metal cations by the sulfate anions. Studies are currently underway in the search for other representatives of (organically) templated mixed-valence transition-metal sulfates as possible magnetic materials.

CONCLUDING REMARKS

The new compound $[CN_3H_6][Fe^{II}Fe^{III}(SO_4)_3(H_2O)_3]$ has a unique structure type characterized by the formation of a 3*D* $[Fe^{II}Fe^{III}(SO_4)_3(H_2O)_3]^-$ framework with layer-by-layer pseudo-2*D* arrangement of the ferric and ferrous cations. Detailed descriptions of the crystal structures of hydrated organo-inorganic sulfates of divalent iron were given in a number of previous works.[12,20,21,24] To date, only one organo-inorganic sulfate $[(CH_3)_2NH_2]_6[Fe^{3+}{}_4Fe^{2+}{}_2(O)_2(OH)_2(SO_4)_8]$ with 2*D* mixed-spin Fe^{II}/Fe^{III} layers is known.[26] In the crystal structure of this compound, the Fe^{2+}- and Fe^{3+}-centered octahedra are connected to each other both via common edges and via common vertices, thus, forming chains.

1 is a structurally novel guanidinium-templated framework related to anhydrous rhombohedral mikasaite $Fe_2(SO_4)_3$.[38] The removal of one of the sulfate tetrahedra and the partial replacement of the Fe^{3+} cations in the $[Fe^{3+}{}_2(SO_4)_3]^0$ framework by Fe^{2+} cations provide the negative charge and allow the incorporation of the protonated organic species in the voids. This structural mechanism known as "stuffed

https://doi.org/10.1021/acs.inorgchem.3c02109
Inorg. Chem. XXXX, XXX, XXX−XXX

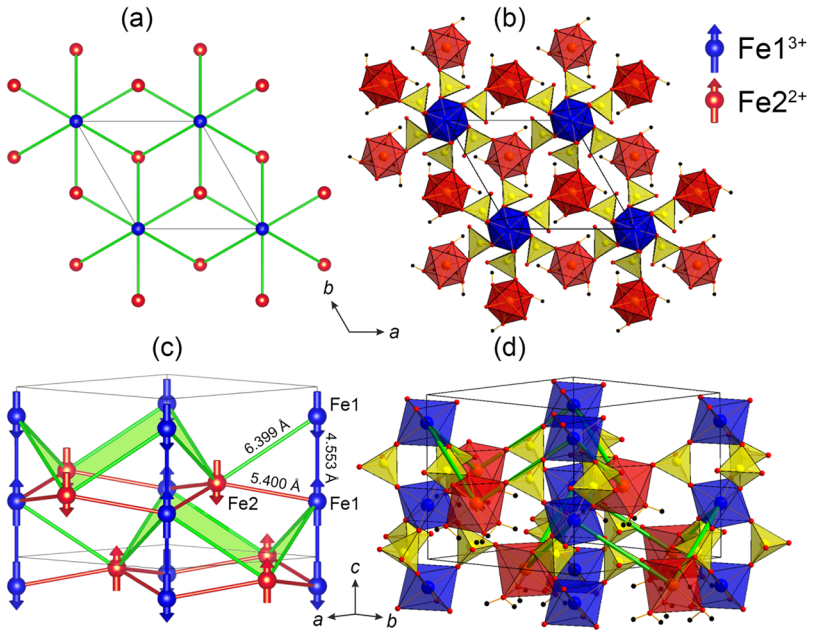

Figure 9. Fragments of the crystal structure of **1** in the (a, b) *ab* plane and (c, d) magnetic structure with J_1 (dark blue), J_2 (red), and J_3 (green) exchange interactions (the direction of the spins has been chosen arbitrarily). Relative spin arrangement is based on the calculated exchange couplings, and the *c*-axis is chosen as the spin direction.

derivative structures," was first described for silicate minerals.[52] Regardless of the several substitutions observed in **1**, its general structural motif and symmetry are related to those of parent $Fe_2(SO_4)_3$. **1** is also structurally related to several representatives of the large family of NASICON-related phases[53,54] and minerals.[55]

As a result of the obtained data of crystal structure analysis, UV−vis−NIR and Mössbauer spectroscopy, as well as magnetic measurements and DFT calculations of **1**, $Fe1^{III}$ and $Fe2^{II}$ can be divided into two independent sites between which insignificant intervalence charge transfer of class II is possible.

Fe1 and Fe2 are ordered well in the crystal structure of **1** and form honeycomb pseudolayers. The presence of the multivalent iron renders these layers ferrimagnetic because of the antiferromagnetic coupling J_3 between Fe^{3+} and Fe^{2+}. The interlayer coupling J_1 leads to a fully compensated magnetic structure. However, signatures of the exchange bias effect may be repercussions of the mixed Fe valence and ferrimagnetism, which is expected within individual layers. The mixing of Fe^{II} and Fe^{III} can be a promising strategy for the design of new magnetic systems.

■ ASSOCIATED CONTENT

Supporting Information

The Supporting Information is available free of charge at https://pubs.acs.org/doi/10.1021/acs.inorgchem.3c02109.

Tables with crystallographic data, selected bond distances and bond valence sums, Rietveld refinement plot, IR and Raman spectra, and Thermal Analysis (TG + DSC) (PDF)

Accession Codes

CCDC 2265854 contains the supplementary crystallographic data for this paper. These data can be obtained free of charge via www.ccdc.cam.ac.uk/data_request/cif, or by emailing data_request@ccdc.cam.ac.uk, or by contacting The Cambridge Crystallographic Data Centre, 12 Union Road, Cambridge CB2 1EZ, UK; fax: +44 1223 336033.

■ AUTHOR INFORMATION

Corresponding Author

Oleg I. Siidra − *Department of Crystallography, St. Petersburg State University, St. Petersburg 199034, Russia; Kola Science Center, Russian Academy of Sciences, Murmansk Region 184200, Russia;* orcid.org/0000-0003-1908-3152; Email: o.siidra@spbu.ru

Authors

Victoria A. Ginga − *Felix Bloch Institute for Solid-State Physics, Leipzig University, Leipzig 04103, Germany; Department of Crystallography, St. Petersburg State University, St. Petersburg 199034, Russia*

Alexander A. Tsirlin − *Felix Bloch Institute for Solid-State Physics, Leipzig University, Leipzig 04103, Germany;* orcid.org/0000-0001-6916-8256

Annette Setzer − *Felix Bloch Institute for Solid-State Physics, Leipzig University, Leipzig 04103, Germany*

Dmitri O. Charkin − *Department of Chemistry, Moscow State University, Moscow 119991, Russia*

Martin Börner − *Institute for Inorganic Chemistry, Leipzig University, Leipzig 04103, Germany*

Veronika R. Abdulina − *Department of Crystallography, St. Petersburg State University, St. Petersburg 199034, Russia*

Semen A. Ivanov − *Department of Chemistry, Moscow State University, Moscow 119991, Russia*

Darya A. Gorbachevskaya − *Department of Crystallography, St. Petersburg State University, St. Petersburg 199034, Russia*

Nikita A. Zolotov − *Institute of Precambrian Geology and Geochronology, Russian Academy of Sciences, St. Petersburg 199034, Russia*

Complete contact information is available at: https://pubs.acs.org/10.1021/acs.inorgchem.3c02109

https://doi.org/10.1021/acs.inorgchem.3c02109
Inorg. Chem. XXXX, XXX, XXX−XXX

Notes

The authors declare no competing financial interest.

■ ACKNOWLEDGMENTS

V.A.G. was financially supported by DAAD (grant # 91837667). Technical support by the SPbSU Resource Centres is gratefully acknowledged.

■ REFERENCES

(1) Brimblecombe, P. The global sulfur cycle. In *treatise on geochemistry*, 2nd ed.; Holland, H. D.; Turekian, K. K., Eds. Elsevier: Oxford, UK.,2013, 559−591 .
(2) Yang, T.; Chou, Y.-M.; Ferré, E. C.; Dekkers, M. J.; Chen, J.; Yeh, E.-C.; Tanikawa, W. Faulting processes unveiled by magnetic properties of fault rocks. *Rev. Geophys.* **2020**, *58* (4), No. e2019RG000690.
(3) Bauer, A.; Velde, B. D. *Geochemistry at the Earth's surface*. Springer-Verlag: Berlin Heidelberg, 2014, 315.
(4) McCord, T. B.; Hansen, G. B.; Matson, D. L.; Johnson, T. V.; Crowley, J. K.; Fanale, F. P.; Carlson, R. W.; Smythe, W. D.; Martin, P. D.; Hibbitts, C. A.; Granahan, J. C.; Ocampo, A. Hydrated salt minerals on Europa's surface from the Galileo near-infrared mapping spectrometer (NIMS) investigation. *J. Geophys. Res.* **1999**, *104*, 11827−11851.
(5) Kargel, J. S. Brine volcanism and the interior structures of asteroids and icy satellites. *Icarus* **1991**, *94*, 368−390.
(6) Bishop, J. L.; Darby Dyar, M.; Lane, M. D.; Banfield, J. F. Spectral identification of hydrated sulfates on Mars and comparison with acidic environments on Earth. *Int. J. Astrobiol.* **2005**, *3*, 275−285.
(7) Zhang, Y.; Cremer, P. Interactions between macromolecules and ions: the Hofmeister series. *Curr. Opin. Chem. Biol.* **2006**, *10*, 658−663.
(8) Boldyrev, A. I.; Simons, J. Isolated SO_4^{2-} and PO_4^{3-} anions do not exist. *J. Phys. Chem.* **1994**, *98*, 2298−2300.
(9) Blades, A. T.; Kebarle, P. Study of the Stability and Hydration of Doubly Charged Ions in the Gas Phase: SO_4^{2-}, $S_2O_6^{2-}$, $S_2O_8^{2-}$, and Some Related Species. *J. Am. Chem. Soc.* **1994**, *116*, 10761−10766.
(10) Wang, X.-B.; Nicholas, J. B.; Wang, L.-S. Electronic Instability of Isolated SO_4^{2-} and Its Solvation Stabilization. *J. Chem. Phys.* **2000**, *113*, 10837−10840.
(11) Kulichenko, M.; Fedik, N.; Bozhenko, K. V.; Boldyrev, A. I. Hydrated Sulfate Clusters $SO_4^{2-}(H_2O)_n$ (n = 1−40): Charge Distribution Through Solvation Shells and Stabilization. *J. Phys. Chem. B* **2019**, *123* (18), 4065−4069.
(12) Fu, Y.; Xu, Z.; Ren, J.; Wu, H.; Yuan, R. Organically Directed Iron Sulfate Chains: Structural Diversity Based on Hydrogen Bonding Interactions. *Inorg. Chem.* **2006**, *45*, 8452−8458.
(13) Angyal, S. J.; Warburton, W. K. 549. The basic strengths of methylated guanidines. *J. Chem. Soc.* **1951**, 2492−2494.
(14) Szafrański, M. Simple Guanidinium Salts Revisited: Room-Temperature Ferroelectricity in Hydrogen-Bonded Supramolecular Structures. *J. Phys. Chem. B* **2011**, *115*, 8755−8762.
(15) Sadman, K.; Wang, Q.; Shull, K. R. Guanidinium Can Break and Form Strongly Associating Ion Complexes. *ACS Macro Lett.* **2019**, *8*, 117−122.
(16) Wu, C.; Jiang, X.; Wang, Z.; Sha, H.; Lin, Z.; Huang, Z.; Long, X.; Humphrey, M. G.; Zhang, C. UV Solar-Blind-Region PhaseMatchable Optical Nonlinearity and Anisotropy in a π-Conjugated Cation-Containing Phosphate. *Angew. Chem., Int. Ed.* **2021**, *60*, 14806−14810.
(17) Wang, D.; Wei, Z.; Bai, Z.; Liu, L.; Lin, Z.; Zhang, L. Hybrid organic-inorganic triguanidine arsenate dihydrate for ultraviolet nonlinear optical application. *Dalton Trans.* **2022**, *51*, 463−467.
(18) Bai, Z.; Liu, L.; Lin, Z.; Ok, K. M. $[C(NH_2)_3]_2Zn(CO_3)_2$: A Guanidinium-Templated Ultraviolet Nonlinear Optical Material. *Inorg. Chem.* **2022**, *61* (31), 12473−12480.
(19) Liu, M.; Ouyang, Z.; Liu, X.; Cao, J.; Xiao, T.; Xia, Z.; Wang, Z. Structure and magnetism of an ideal one-dimensional chain antiferromagnet $[C_2NH_8]_3[Fe(SO_4)_3]$ with a large spin of S = 5/2. *Inorg. Chem.* **2022**, *61* (38), 15045−15050.
(20) Paul, G.; Choudhury, A.; Rao, C. N. R. Organically Templated Linear and Layered Iron Sulfates. *Chem. Mater.* **2003**, *15* (5), 1174−1180.
(21) Rao, C. N. R.; Sampathkumaran, E. V.; Nagarajan, R.; Paul, G.; Behera, J. N.; Choudhury, A. Synthesis, Structure, and the Unusual Magnetic Properties of an Amine-Templated Iron(II) Sulfate Possessing the Kagomé Lattice. *Chem. Mater.* **2004**, *16* (8), 1441−1446.
(22) Fanfani, L.; Nunzi, A.; Zanazzi, P. F. The crystal structure of roemerite. *Am. Mineral.* **1970**, *55* (1−2), 78−89.
(23) Goßner, B.; Fell, E. Sulfates of the voltaite type. *Ber. Dtsch. Chem. Ges.* **1932**, *65*, 393−395.
(24) Fleck, M.; Bohatý, L.; Tillmanns, E. Structural characterisation of MII guanidinium sulphate hydrates (M^{II}=Mn,Fe,Co,Ni,Cd,VO). *Solid State Sci.* **2004**, *6* (5), 469−477.
(25) Li, C. R.; Li, S. L.; Zhang, X. M. D_3-symmetric supramolecular cation $\{(Me_2NH_2)_6(SO_4)\}^{4+}$ as a new template for 3D homochiral (10,3)-a metal oxalates. *Cryst. Growth & Design.* **2009**, *9* (4), 1702−1707.
(26) Sorolla, M.; Wang, X.; Kubíčková, L.; Ksenofontov, V.; Möller, A.; Jacobson, A. J. A Mixed-valent iron (II/III) diamond chain with single-ion anisotropy. *Inorg. Chem.* **2020**, *59* (2), 1068−1074.
(27) DeBord, J. R. D.; Reiff, W. M.; Warren, C. J.; Haushalter, R. C.; Zubieta, J. A 3-D Organically Templated Mixed Valence (Fe^{2+}/Fe^{3+}) Iron Phosphate with Oxide-Centered $Fe_4O(PO_4)_4$ Cubes: Hydrothermal Synthesis, Crystal Structure, Magnetic Susceptibility, and Mössbauer Spectroscopy of $[H_3NCH_2CH_2NH_3]_2[Fe_4O(PO_4)_4]\cdot H_2O$. *Chem. Mater.* **1997**, *9* (9), 1994−1998.
(28) Kai-Lun, Y.; Jian-Wen, L.; Zu-Li, L.; Hua-Hua, F.; Lin, Z. Magnetic properties of a mixed spin-2 and spin-5/2 Heisenberg ferrimagnetic system on a two-dimensional honeycomb lattice: Green's function approach. *Commun. Theor. Phys.* **2007**, *47* (4), 741−746.
(29) Sheldrick, G. M. Crystal structure refinement with SHELXL. *Acta Crystallogr. Sect. C: Struct. Chem.* **2015**, *C71*, 3−8.
(30) Petříček, V.; Dušek, M.; Palatinus, L. Crystallographic computing system JANA2006: General features. *Z. Krist.-Cryst. Mater.* **2014**, *229*, 345−352.
(31) Rietveld, H. M. A profile refinement method for nuclear and magnetic structures. *J. Appl. Crystallogr.* **1969**, *2* (2), 65−71.
(32) Wesley, W. M.; Harry, W. G. H. *Reflectance Spectroscopy*. Wiley: New York, 1966, 104−169.
(33) Kresse, G.; Furthmüller, J. Efficiency of ab-initio total energy calculations for metals and semiconductors using a plane-wave basis set. *Comput. Mater. Sci.* **1996**, *6* (1), 15−50.
(34) Kresse, G.; Furthmüller, J. Efficient iterative schemes for ab initio total-energy calculations using a plane-wave basis set. *Phys. Rev. B* **1996**, *54* (16), 11169−11186.
(35) Perdew, J. P.; Burke, K.; Ernzerhof, M. Generalized Gradient Approximation Made Simple. *Phys. Rev. Lett.* **1996**, *77* (18), 3865−3868.
(36) Tsirlin, A. A.; Rousochatzakis, I.; Filimonov, D.; Batuk, D.; Frontzek, M.; Abakumov, A. M. Spin-reorientation transitions in the Cairo pentagonal magnet $Bi_4Fe_5O_{13}F$. *Phys. Rev. B* **2017**, *96* (9), No. 094420.
(37) Xiang, H. J.; Kan, E. J.; Wei, S.-H.; Whangbo, M.-H.; Gong, X. G. Predicting the spin-lattice order of frustrated systems from first principles. *Phys. Rev. B* **2011**, *84*, No. 224429.
(38) Masse, R.; Guitel, J. C.; Perret, R. Structure crystalline de la variéte rhomboédrique du sulfate ferrique $Fe_2(SO_4)_3$. *Bull. Soc. Fr. Minéral. Cristallogr.* **1973**, *96*, 346−349.
(39) Rossman, G. R.; Ehlmann, B. L. In *Remote Compositional Analysis: Techniques for Understanding Spectroscopy, Mineralogy, and Geochemistry of Planetary Surfaces*; Eds. Bishop, J. L.; Bell, III, J. F.; Moersch, J. E. Cambridge Planetary Science, Cambridge University Press: Cambridge, 2019, 3−20 .

https://doi.org/10.1021/acs.inorgchem.3c02109
Inorg. Chem. XXXX, XXX, XXX−XXX

(40) Fontana, I.; Lauria, A.; Spinolo, G. Optical Absorption Spectra of Fe^{2+} and Fe^{3+} in Aqueous Solutions and Hydrated Crystals. *Phys. Status Solidi B* **2007**, *244*, 4669−4677.
(41) Cotton, F. A.; Myers, M. D. Magnetic and Spectral Properties of the Spin-Free $3d^6$ Systems Iron(II) and Cobalt(III) in Cobalt(III) Hexafluoride Ion: Probable Observation of Dynamic Jahn−Teller Effects. *J. Am. Chem. Soc.* **1960**, *82*, 5023−5026.
(42) Robin, M. B.; Day, P. Mixed−Valence Chemistry−A Survey and Classification. *Adv. Inorg. Chem. Radiochem.* **1968**, *10*, 247−423.
(43) Dyar, M. D.; Breves, E.; Jawin, E.; Marchand, G.; Nelms, M.; O'Connor, V.; Peel, S.; Rothstein, Y.; Sklute, E. C.; Lane, M. D.; Bishop, J. L.; Mertzman, S. A. Mossbauer parameters of iron in sulfate minerals. *Am. Mineral.* **2013**, *98* (11−12), 1943−1965.
(44) Huggins, G. P.; Huffman, F. E. Chapter 50 - Mössbauer analysis of iron-bearing phases in coal, coke, and ash. *Analytic. Methods Coal Coal Prod.* **1979**, *3*, 371−423.
(45) Majzlan, J.; Schlicht, H.; Wierzbicka-Wieczorek, M.; Giester, G.; Pöllmann, H.; Brömme, B.; Doyle, S.; Buth, G.; Bender Koch, C. A contribution to the crystal chemistry of the voltaite group: solid solutions, Mössbauer and infrared spectra, and anomalous anisotropy. *Mineral. Petrol.* **2013**, *107*, 221−233.
(46) Long, G. J.; Longworth, G.; Day, P.; Beveridge, D. A Mössbauer-effect study of the electronic and magnetic properties of voltaite, a mixed-valence mineral. *Inorg. Chem.* **1980**, *19*, 821−829.
(47) Majzlan, J.; Alpers, C. N.; Koch, C. B.; McCleskey, R. B.; Myneni, S. C. B.; Neil, J. M. Vibrational, X-ray absorption, and Mössbauer spectra of sulfate minerals from the weathered massive sulfide deposit at Iron Mountain, California. *Chem. Geol.* **2011**, *284*, 296−305.
(48) Stamps, R. L. Mechanisms for exchange bias. *J. Phys. D: Appl. Phys.* **2000**, *33*, R247.
(49) Gondh, S.; Patidar, M. M.; Kumar, K.; Saravanan, M. P.; Ganesan, V.; Pramanik, A. K. Large exchange bias and low-temperature glassy state in the frustrated triangular-lattice antiferromagnet $Ba_3NiIr_2O_9$. *Phys. Rev. B* **2021**, *104*, No. 014401.
(50) Deng, Z.; Wang, X.; Wang, M.; Shen, F.; Zhang, J.; Chen, Y.; Feng, H. L.; Xu, J.; Peng, Y.; Li, W.; Zhao, J.; Wang, X.; Valvidares, M.; Francoual, S.; Leupold, O.; Hu, Z.; Tjeng, L. H.; Li, M.; Croft, M.; Zhang, Y.; Liu, E.; He, L.; Hu, F.; Sun, J.; Greenblatt, M.; Jin, C. Giant Exchange-Bias-Like Effect at Low Cooling Fields Induced by Pinned Magnetic Domains in Y_2NiIrO_6 Double Perovskite. *Adv. Mater.* **2023**, *35*, 2209759.
(51) Nakamura, Y. Existence of a compensation temperature of a mixed spin-2 and spin-5/2 Ising ferrimagnetic system on a layered honeycomb lattice. *Phys. Rev. B* **2000**, *62* (17), 11742−11746.
(52) Buerger, M. J. The stuffed derivatives of the silica structures. *Am. Mineral.* **1954**, *39*, 600−614.
(53) Slater, P. R.; Greaves, C. Powder neutron diffraction study of the Nasicon-related phases. $Na_xM^{II}_xM^{III}_{2-x}(SO_4)_{3-y}(SeO_4)y$: M^{II} = Mg, M^{III} = Fe, In. *J. Mater. Chem.* **1994**, *4*, 1469−1473.
(54) Anantharamulu, N.; Koteswara Rao, K.; Rambabu, G.; Vijaya Kumar, B.; Radha, V.; Vithal, M. A wide-ranging review on nasicon type materials. *J. Mater. Sci.* **2011**, *46*, 2821−2837.
(55) Siidra, O. I.; Nazarchuk, E. V.; Zaitsev, A. N.; Vlasenko, N. S. Koryakite, $NaKMg_2Al_2(SO_4)_6$, a new NASICON-related anhydrous sulfate mineral from Tolbachik volcano, Kamchatka, Russia. *Mineral. Mag.* **2020**, *84*, 283−287.

https://doi.org/10.1021/acs.inorgchem.3c02109
Inorg. Chem. XXXX, XXX, XXX−XXX